Research Article | Vol. 9, No. 12 | 1 Dec 2018 | BIOMEDICAL OPTICS EXPRESS 6556
Biomedical Optics EXPRESS

Ultrafast polarization bio-imaging based on coherent detection and time-stretch techniques

LU SONG,[1] YUANHUA FENG,[2,*] XIAOJIE GUO,[1] YUECHENG SHEN,[3] DAIXUAN WU,[3] ZHENHUA WU,[1] CONGRAN ZHOU,[4] LINYAN ZHU,[4] SHECHENG GAO,[2] WEIPING LIU,[2] XUMING ZHANG,[5,6] AND ZHAOHUI LI[3,7]

[1]*Guangdong Provincial Key Laboratory of Optical Fiber Sensing and Communications, Institute of Photonics Technology, Jinan University, Guangzhou 510632, China*
[2]*Department of Electronic Engineering, College of Information Science and Technology, Jinan University, Guangzhou 510632, China*
[3]*School of Electronics and Information Technology, Sun Yat-Sen University, Guangzhou 510006, China*
[4]*Department of Pharmacology, School of Medicine, Jinan University, Guangzhou 510632, China*
[5]*Department of Applied Physics, The Hong Kong Polytechnic University, Hong Kong, China*
[6]*apzhang@polyu.edu.hk*
[7]*lzhh88@mail.sysu.edu.cn*
**favinfeng@163.com*

Abstract: Optical polarization imaging has played an important role in many biological and biomedical applications, as it provides a label-free and non-invasive detection scheme to reveal the polarization information of optical rotation, birefringence, and photoelasticity distribution inherent in biological samples. However, the imaging speeds of the previously demonstrated polarization imaging techniques were often limited by the slow frame rates of the arrayed imaging detectors, which usually run at frame rates of several hundred hertz. By combining the optical coherent detection of orthogonal polarizations and the optical time-stretch imaging technique, we achieved ultrafast polarization bio-imaging at an extremely fast record line scanning rate up to 100 MHz without averaging. We experimentally demonstrated the superior performance of our method by imaging three slices of different kinds of biological samples with the retrieved Jones matrix and polarization-sensitive information including birefringence and diattenuation. The proposed system in this paper may find potential applications for ultrafast polarization dynamics in living samples or some other advanced biomedical research.

1. Introduction

Optical polarization imaging detects the changes in the polarization states of light after passing through or being reflected by polarization-sensitive samples through a combination of a polarizer and an analyzer [1]. These changes, which are normally related to optical rotation, birefringence, and photoelastic effect, are difficult to be detected or sensed using conventional light intensity- and phase-based imaging systems [2]. Especially in many biological and biomedical applications, such as bulk tissue characterization [3,4], normal and cancerous cells differentiation [5] and *in-vivo* microcirculation studying [6], optical polarization imaging has becoming a promising detecting and analyzing approach with the advantages of label-free, non-invasion, low damage to samples and sensitive to sub-wavelength structures [7].

To date, several different polarization imaging approaches have been proposed or demonstrated, including conventional single polarized light microscopy [8,9], two polarized lights based Jones matrix microscopy [10] and multiple polarized lights based Mueller matrix imaging system [11]. Apart from static biological sample, optical polarization imaging was further extended to observe the dynamic processes, from macroscopic to microscopic like the

#347625 https://doi.org/10.1364/BOE.9.006556
Journal © 2018 Received 8 Oct 2018; revised 22 Nov 2018; accepted 23 Nov 2018; published 29 Nov 2018

Biomedical Optics EXPRESS

birefringence change of a muscle tissue [12] to the dynamics of microtubules and molecules [13,14], from plant to animal like the expansion of a plant cell wall [15] to the dynamics of an animal living cell [16]. However, in almost all previous polarization imaging techniques the mainly used wide-field light arrayed detectors, such as charge-coupled device (CCD) or complementary metal-oxide semiconductor (CMOS) camera, usually suffer from low frame rates while maintain large pixel counts [17], therefore significantly restricting the imaging speed of the polarization imaging techniques. Since imaging polarization information with an ultrahigh temporal resolution is essential in understanding ultrafast polarization-sensitive dynamics, developing an ultrafast polarization imaging system is highly desirable.

Optical ultrafast time-stretch imaging has been an emerging method that achieves an ultrahigh temporal resolution [18]. The essential principle of ultrafast time-stretch imaging includes three steps. Firstly, the spatial information of the sample is encoded into the spectrum of a femtosecond laser pulse through a spatial disperser. Secondly, the modulated laser pulse is stretched into a temporal waveform whose power distribution is proportional to its spectral intensity. Finally, a high-speed optoelectronic detector captures the temporal waveform, which will be processed for image reconstruction. By taking advantage of high-speed optoelectronic components and demodulation techniques in modern optical communication, time-stretch imaging provides a unique way to obtain ultrafast information up to 100 million frames per second. Using time-stretch imaging techniques, several applications have been demonstrated, such as ultrafast tissue and particles imaging, high throughput cell screening, and cellular drug analysis [18–22]. However, all these demonstrated time-stretch imaging modalities above focus on either light intensity or phase detection, while a time-stretch imaging modality based on light polarization has not yet been reported.

In this paper, we present a coherent detection and time-stretch based ultrafast polarization imaging system that is capable of delivering spatially dependent Jones matrix of biological samples with a record line scanning rate up to 100 MHz without averaging. Such a capability is enabled by combining an optical coherent detection of orthogonal polarizations and a time-stretch technique. Using a phase and polarization diversified homodyne coherent receiver, the imaging system can extract the full field information, including the amplitude, phase, and state of polarization [23], of the light after probing the sample. Thus, all the elements in the Jones matrix of the sample could be directly retrieved, as well as the polarization parameters including diattenuation and birefringence-related phase retardation.

2. Methods

2.1 Principle and experimental setup

With the capability of determining complete information of the electric field, the Jones matrix imaging is able to provide polarization-sensitive information [24]. To obtain the Jones matrix of the targeted biological sample, two independent incident polarization states are required in the imaging system [25]. In our system, we chose two linear polarization states that are orthogonal to each other, which are referred to as *x*- and *y*-polarizations in the rest of the paper. The setup for our ultrafast polarization imaging system is shown in Fig. 1(a), which incorporates the polarization-division multiplexing and coherent detection technique. The optical coherent receiver utilized here consists of two homodyne coherent receivers in a polarization diversity configuration [20] as shown in Fig. 1(b). An optical local oscillator (LO) is required as an absolute phase and polarization reference to restore the phase and polarization information of the incoming optical signal. A polarization beam splitter (PBS) is first used to separate the optical LO and signal into two linear orthogonal polarization components, which are then detected by two homodyne coherent receivers. Based on a 90° optical hybrid and balanced photodetectors, homodyne receiver could output in-phase (I) and quadrature (Q) component of the interference term of the optical LO and signal. I and Q component can then be digitized and used to restore complex full information on the optical

Biomedical Optics EXPRESS

complex amplitude and the state of the polarization. An optical coherent receiver based ultrafast quantitative phase imaging has been demonstrated in our previous work [26], where only a single polarized input was used. The details of the proposed imaging system and the operating procedures are described as follows.

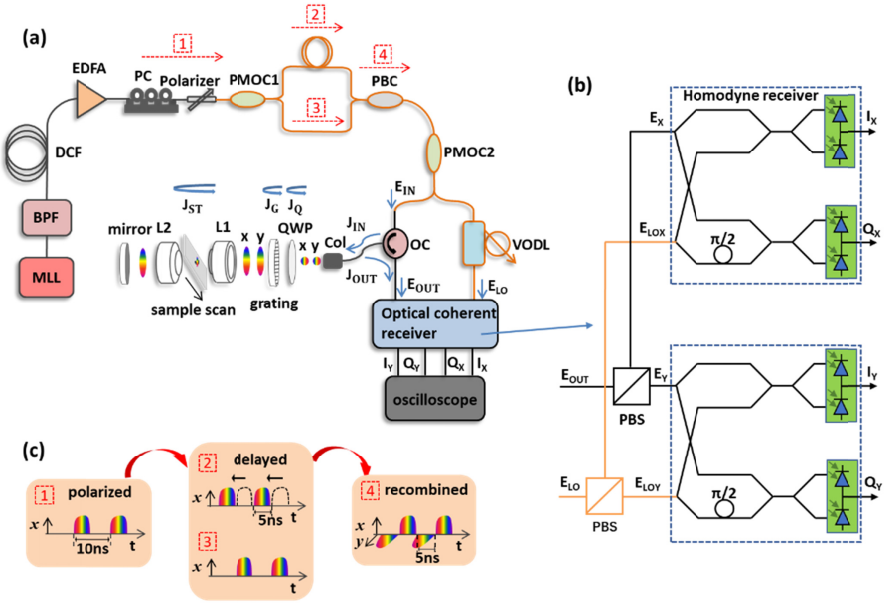

Fig. 1. (a) Schematic setup of our ultrafast polarization imaging system. (b) Schematic diagram of the optical coherent receiver. (c) Step-by-step illustrations of the polarization-division multiplexing. MLL: mode-locked laser; BPF: band pass filter; DCF: dispersion compensating fiber; EDFA: erbium-doped fiber amplifier; PC: polarization controller; PMOC: polarization maintaining optical coupler; PBC: polarization beam combiner; OC: optical circulator; VODL: variable optical delay line; Col: collimator; QWP: quarter wave plate; L1, L2: objective lenses; all the orange-colored components are polarization maintaining (PM) fiber devices.

A home-made mode-locked laser (MLL) generated an optical pulse train with a repetition rate of 100 MHz and a pulse width of ~100 fs. These pulses were then filtered around 1550 nm with a 14-nm bandwidth. After passing through a dispersive fiber with 330 ps/nm group velocity dispersion (GVD), the pulses were dispersed to about 4.6 ns wide. An Erbium-doped fiber amplifier (EDFA) was used to amplify the average power to 20 dBm, which compensates the energy loss during dispersion. The processes to generate two linear orthogonal polarized beams are labeled with 1-4 in Fig. 1(a), and a detailed illustration of each process is depicted in Fig. 1(c). In process 1, a combination of a polarization controller (PC) and an in-line fiber polarizer was firstly used to make the dispersed pulse train become linear polarized, and to ensure its polarization direction in alignment with the slow axis of the fiber polarizer. Then, a polarization maintaining optical coupler (PMOC) with 50:50 power splitting ratio separated the pulses into two arms. In processes 2 and 3, compared to the pulses in the lower arm, the pulses in the upper arm were temporal delayed about 5 ns by using length designed PM optical fibers. More specifically, pulses in both arms still travelled along the slow axis of the PM fiber. Then, the pulses in the upper arm and lower arm were recombined through a polarization beam combiner (PBC). Thus, in process 4, we got temporal interlaced pulse train with alternative orthogonal polarizations travelling just along the fast and slow axes of the PM fiber of PBC. After that, a 1 × 2 PMOC separated the pulses into a signal beam and a local oscillator (LO) with a 75:25 power splitting ratio. These PM devices above are necessary for maintaining a stable polarization state of the signal and LO light. An optical circulator (OC) was used to direct the input signal beam to the sample and

Biomedical Optics EXPRESS

couple the output signal beam out for measurement. In the signal beam, a fiber collimator was used to couple light from the fiber to free space. A quarter wave plate (QWP) was inserted and adjusted to guarantee that successive pulses maintained linear orthogonal polarizations. Then, the pulses in the signal beam were spatially dispersed into a one-dimensional (1-D) spectral rainbow by a volume holographic transmission diffraction grating (Wasatch Photonics, spatial frequency = 600 lines/mm). Therefore, the spatial information of the sample was encoded into the spectrum of the pulse and the average light power illuminating on sample is about 10mW. After interacting with the sample twice (reflection mode with a mirror, Fig. 1(a)), the signal beam that contains the sample information mixed with the LO and detected by an optical digital coherent receiver. A PM variable optical delay line (VODL) in the LO arm was used to fine tune the relative time delay which determines the beat frequency between signal and LO pulses. A real-time oscilloscope (LeCroy LabMaster 10Zi) with a sampling rate of 80 GS/s was used to digitize and acquire the I and Q data of the orthogonal polarization signal from the receiver. I and Q data was sent to a computer to reconstruct the Jones matrix of the sample. The polarizing effects of the sample, including retardance and diattenuation, can be fully characterized and extracted from the retrieved Jones matrix. Our system is a 1D line scan imaging system, this 1D line scan achieved by the spatial dispersion and temporal dispersion of the chirped laser pulse. Thus, the frame rate of this system depends on the pulse repetition of the laser source, i.e. 100MHz. However, it's worth mentioning that the whole exhausting recording time (~200ms) for one line scanning is much longer than the line scanning period (10ns), which is mainly hindered by the data transfer time between computer and the real time oscilloscope. This has no effect on the demonstration of the proposed imaging system. The 2D image acquirement needs the vertical scanning. Therefore, the imaging field of view (FOV) and resolution along the horizontal and vertical direction depend on different factors. The horizontal imaging FOV is up to the length of the 1D dispersed illumination light spot, which mainly depends on the filtered wavelength bandwidth, the spatial frequency of diffraction grating and the NA of the objective lens [27], while the vertical imaging FOV depends on the scanning speed. In addition, the horizontal spatial resolution, which depends on the spatial frequency of diffraction grating, the GVD of the dispersion compensating fiber, and the digitized bandwidth of the coherent receiver [27], is 3μm, nearly the same with the previous system [26]. The vertical spatial resolution which only depends on the NA of the objective lens is higher than the horizontal resolution.

2.2 Jones matrix analysis

Having described the system setup and the operating procedures, we provide a detailed analysis for reconstructing the Jones matrix of the sample. The Jones vector ($\boldsymbol{E}_{IN}$) of the input signal beam is transformed into the output Jones vector ($\boldsymbol{E}_{OUT}$) by

$$\boldsymbol{E}_{OUT} = \boldsymbol{J}_{OUT}\boldsymbol{J}_{QB}\boldsymbol{J}_{GB}\boldsymbol{J}_{ST}\boldsymbol{J}_{GI}\boldsymbol{J}_{QI}\boldsymbol{J}_{IN}\boldsymbol{E}_{IN} \tag{1}$$

where $\boldsymbol{J}_{IN}$ and $\boldsymbol{J}_{OUT}$ represent the Jones matrices of the input and output optical fibers at the signal beam respectively, $\boldsymbol{J}_{ST}$ is the round-trip Jones matrix of the sample, $\boldsymbol{J}_{QI}$ and $\boldsymbol{J}_{QB}$ are the Jones matrices of the QWP for incident and back reflected lights, respectively, $\boldsymbol{J}_{GI}$ and $\boldsymbol{J}_{GB}$ are the Jones matrices of the grating for incident and back reflected light, respectively. According to the Jones reversibility theorem [28], we know

$$\boldsymbol{J}_{GB} = \boldsymbol{J}_{GI}^{T}, \boldsymbol{J}_{QB} = \boldsymbol{J}_{QI}^{T} \tag{2}$$

where the symbol T stands for taking the transpose of a matrix. Here, the input SMF fiber length of OC is about 2 meters, and we have tapped it onto the optical table in the experiment, thus the diattenuation of the input SMF fiber can be ignored, then the Jones matrix of the input fiber, $\boldsymbol{J}_{IN}$, can be modeled as linear retarder [29]. The Jones matrix of the QWP, $\boldsymbol{J}_{QI}$, is also a linear retarder with adjustable angle. Therefore, we can use the QWP to compensate for

Biomedical Optics EXPRESS

the elliptical polarization transformation induced by the input fiber and make the incident pulses before the grating maintaining linear. With a specific adjusted angle of the optic axis of the QWP, the $\boldsymbol{J}_{IN}$ and $\boldsymbol{J}_{QI}$ can have a relationship as follows:

$$\boldsymbol{J}_{QI} = \boldsymbol{J}_{IN}^{-1} \tag{3}$$

The utilized diffraction grating has a diffraction efficiency (η) of 90% around 1550 nm. While the phase retardation induced by the grating of linear orthogonal polarized lights may be different, we can still express $\boldsymbol{J}_{GI}$ as $\left[\sqrt{\eta},0;0,\sqrt{\eta}e^{i\varphi_g}\right]$, where φ_g is the phase retardation difference between the linear orthogonal polarized lights induced by the grating. With equations above, we can rewrite the Eqs. (1) into,

$$\begin{aligned}\boldsymbol{E}_{OUT} &= \boldsymbol{J}_{OUT}\boldsymbol{J}_{QB}\boldsymbol{J}_{GB}\boldsymbol{J}_{ST}\boldsymbol{E}_{IN'}\\ \boldsymbol{E}_{IN'} &= \boldsymbol{J}_{GI}\boldsymbol{J}_{QI}\boldsymbol{J}_{IN}\boldsymbol{E}_{IN}\end{aligned} \tag{4}$$

where $\boldsymbol{E}_{IN'}$ represents the electric fields of input pulses after the grating, with its polarization linear orthogonal. The electric fields of the incident pulses with linear orthogonal polarization states are denoted as $\boldsymbol{E}_{INx}$ and $\boldsymbol{E}_{INy}$. Although pulses with linear orthogonal polarizations are temporally separated, we incorporate them into a single matrix for mathematical convenience, as follows:

$$\boldsymbol{E}_{IN'} = \sqrt{\eta}\left[\boldsymbol{E}_{INx} \quad \boldsymbol{E}_{INy}\right] = \sqrt{\eta}\begin{bmatrix}1 & 0\\ 0 & e^{i\varphi}\end{bmatrix} \tag{5}$$

where φ is the relative phase difference between the two linear orthogonal polarized pulses after the grating, it is induced by the grating and the different travelling length in process 2 and 3.

A digital coherent receiver was used to measure the interferometric signals. For each polarized pulse, the coherent receiver output I_{iX}, Q_{iX}, I_{iY}, and Q_{iY} ($i = x, y$) from four channels, where X and Y are referred to as two orthogonal polarization components of the coherent receiver. Here, I_{iX} and Q_{iX} correspond to the in-phase and quadrature part of the interference term of the X component in the coherent receiver of the i-polarized pulse ($i = x, y$), while I_{iY} and Q_{iY} correspond to the in-phase and quadrature part of the interference term of the Y component in the coherent receiver. After getting the output data of orthogonal polarized pulses, we can form an $\boldsymbol{S}$ matrix based on the digital coherent measurement [30].

$$\begin{aligned}\boldsymbol{S} &= \begin{bmatrix}I_{xX}+i\cdot Q_{xX} & I_{yX}+i\cdot Q_{yX}\\ I_{xY}+i\cdot Q_{xY} & I_{yY}+i\cdot Q_{yY}\end{bmatrix} = R\begin{bmatrix}E_{LOX}^{*} & 0\\ 0 & E_{LOY}^{*}\end{bmatrix}\boldsymbol{E}_{OUT}\\ &= R\sqrt{\eta}\begin{bmatrix}E_{LOX}^{*} & 0\\ 0 & E_{LOY}^{*}\end{bmatrix}\boldsymbol{J}_{OUT}\boldsymbol{J}_{QB}\boldsymbol{J}_{GB}\boldsymbol{J}_{ST}\boldsymbol{E}_{IN'}\end{aligned} \tag{6}$$

Here, R represents the responsivity of the photodiode. E_{LOX} and E_{LOY} are the X and Y electric fields components of the LO pulse in the coherent receiver. The linear orthogonal polarized pulses in the LO arm transmit along the fast and slow axis of the PM fiber, and when it reaches the coherent receiver, the linear orthogonal polarized pulses split equally into the X and Y channels of the detector. Thus, we can write the Jones matrix of digital coherent as

$$\begin{bmatrix}E_{LOX}^{*} & 0\\ 0 & E_{LOY}^{*}\end{bmatrix} = \frac{\sqrt{P}}{2}\begin{bmatrix}1 & 0\\ 0 & e^{i\varphi_1}\end{bmatrix} \tag{7}$$

Biomedical Optics EXPRESS

Here, φ_1 is the relative phase difference between the linear orthogonal polarizations of LO at the coherent receiver, P is the average power of the LO light. With Eq. (7), we can rewrite the Eq. (6) as

$$\boldsymbol{S} = \frac{\sqrt{RP\eta}}{2}\begin{bmatrix}1 & 0\\ 0 & e^{i\varphi_1}\end{bmatrix}\boldsymbol{J}_{OUT}\boldsymbol{J}_{QB}\boldsymbol{J}_{GB}\boldsymbol{J}_{ST}\boldsymbol{E}_{IN'} \tag{8}$$

Similar to the fiber-optic components based polarization-sensitive optical coherence tomography (PS-OCT) system [31], a reference measurement is needed to obtain the round trip Jones matrix of the sample $\boldsymbol{J}_{ST}$. When nothing is placed at the sample position, we assume,

$$\boldsymbol{J}_{\text{ST-ref}} = e^{i\varphi_2}\begin{bmatrix}1 & 0\\ 0 & 1\end{bmatrix} \tag{9}$$

where φ_2 represents the phase delay caused by the free space propagation. Actually, the reference measurement was achieved by a blank line scan imaging, then a whole image could be reconstructed base on it. The blank reference signal can be expressed as

$$\boldsymbol{S}_{ref} = \frac{\sqrt{RP\eta}}{2}e^{i\varphi_2}\begin{bmatrix}1 & 0\\ 0 & e^{i\varphi_1}\end{bmatrix}\boldsymbol{J}_{OUT}\boldsymbol{J}_{QB}\boldsymbol{J}_{GB}\boldsymbol{E}_{IN'} \tag{10}$$

By multiplying the inverse matrix of $\boldsymbol{S}_{ref}$ with $\boldsymbol{S}$, we get,

$$\begin{aligned}\boldsymbol{S}_{ref}{}^{-1}\boldsymbol{S} &= \mathrm{e}^{-i\varphi_2}\boldsymbol{E}_{IN'}^{-1}\boldsymbol{J}_{GB}^{-1}\boldsymbol{J}_{QB}^{-1}\boldsymbol{J}_{OUT}^{-1}\begin{bmatrix}1 & 0\\ 0 & e^{i\varphi_1}\end{bmatrix}^{-1}\frac{2}{\sqrt{RP\eta}}\frac{\sqrt{RP\eta}}{2}\begin{bmatrix}1 & 0\\ 0 & e^{i\varphi_1}\end{bmatrix}\boldsymbol{J}_{OUT}\boldsymbol{J}_{QB}\boldsymbol{J}_{GB}\boldsymbol{J}_{ST}\boldsymbol{E}_{IN'}\\ &= \mathrm{e}^{-i\varphi_2}\boldsymbol{E}_{IN'}^{-1}\boldsymbol{J}_{ST}\boldsymbol{E}_{IN'}\end{aligned} \tag{11}$$

We note that some terms can be canceled out, and we can finally get an explicit expression of the round trip Jones matrix of the sample

$$\boldsymbol{J}_{ST} = \mathrm{e}^{i\varphi_2}\begin{bmatrix}1 & 0\\ 0 & e^{i\varphi}\end{bmatrix}\boldsymbol{S}_{ref}{}^{-1}\boldsymbol{S}\begin{bmatrix}1 & 0\\ 0 & e^{i\varphi}\end{bmatrix}^{-1} = e^{i\varphi_2}\begin{bmatrix}1 & 0\\ 0 & e^{i\varphi}\end{bmatrix}\boldsymbol{S}_{ref}{}^{-1}\boldsymbol{S}\begin{bmatrix}1 & 0\\ 0 & \mathrm{e}^{-i\varphi}\end{bmatrix} \tag{12}$$

We note here that $\mathrm{e}^{i\varphi_2}$ is a constant phase term, which has no influence on retrieving the information of the sample. To solve for the unknown phase φ, we used the fact that the round trip Jones matrix of the sample $\boldsymbol{J}_{ST}$ is a transposed symmetric matrix [32]. Having obtained the round trip Jones matrix of the sample, we can also transform it into an equivalent Mueller matrix [30],

$$M = U(J\otimes J^*)U^{-1} = U\begin{bmatrix}\boldsymbol{J}_{11}\boldsymbol{J}_{11}^* & \boldsymbol{J}_{11}\boldsymbol{J}_{12}^* & \boldsymbol{J}_{12}\boldsymbol{J}_{11}^* & \boldsymbol{J}_{12}\boldsymbol{J}_{12}^*\\ \boldsymbol{J}_{11}\boldsymbol{J}_{21}^* & \boldsymbol{J}_{11}\boldsymbol{J}_{22}^* & \boldsymbol{J}_{12}\boldsymbol{J}_{21}^* & \boldsymbol{J}_{12}\boldsymbol{J}_{22}^*\\ \boldsymbol{J}_{21}\boldsymbol{J}_{11}^* & \boldsymbol{J}_{21}\boldsymbol{J}_{12}^* & \boldsymbol{J}_{22}\boldsymbol{J}_{11}^* & \boldsymbol{J}_{22}\boldsymbol{J}_{12}^*\\ \boldsymbol{J}_{21}\boldsymbol{J}_{21}^* & \boldsymbol{J}_{21}\boldsymbol{J}_{22}^* & \boldsymbol{J}_{22}\boldsymbol{J}_{21}^* & \boldsymbol{J}_{22}\boldsymbol{J}_{22}^*\end{bmatrix}U^{-1} \tag{13}$$

where the $\otimes$ represents the Kronecker tensor product and U is the 4 × 4 Jones–Mueller transformation matrix,

Biomedical Optics EXPRESS

$$\boldsymbol{U} = \frac{1}{\sqrt{2}}\begin{bmatrix} 1 & 0 & 0 & 1 \\ 1 & 0 & 0 & -1 \\ 0 & 1 & 1 & 0 \\ 0 & i & -i & 0 \end{bmatrix} \tag{14}$$

Unlike a Jones matrix, the Mueller matrix can be applied to all kinds of optical system and it shows a more explicit intensity transformation property over the Jones matrix under some situations. For example, M_{11} element represents a complete intensity transformation property of the sample without the influence of polarization property. Having obtained the Jones matrix of the sample, we can use two different methods, matrix diagonalization [31] or polar decomposition [33], to retrieve the polarization parameters, such as diattenuation and phase retardation. It is noted that matrix diagonalization and polar decomposition are equivalent in fact. Based on matrix polar decomposition, we can express retardance (R) and diattenuation (D) with only the Jones matrix and the polarization parameters [33] as,

$$\begin{aligned} D &= \left(1 - \frac{4\left|\det \boldsymbol{J}\right|^2}{\left(tr(\boldsymbol{J}^\dagger \boldsymbol{J})\right)^2}\right)^{1/2} \\ R &= 2\cos^{-1}\left(\frac{\left|tr\boldsymbol{J} + \frac{\det \boldsymbol{J}}{\left|\det \boldsymbol{J}\right|} tr\boldsymbol{J}^\dagger\right|}{2\left(tr\left(\boldsymbol{J}^\dagger \boldsymbol{J}\right) + 2\left|\det \boldsymbol{J}\right|\right)^{1/2}}\right) \end{aligned} \tag{15}$$

where the tr and det are the trace and determinant of the matrix, respectively, the † denotes the conjugate transpose of the matrix.

3. Experimental results

In order to demonstrate the validity of the quantitative polarization information retrieved by the system, we firstly imaged a birefringent resolution target (thorlabs, R2L2S1B) which has two N-BK7 protective glass covers and a liquid crystal polymer layer inside. The fast axis of the liquid crystal polymer layer is designed to aligned parallel to the side of the glass covers. The target has a retardation of 280 ± 20 nm and a maximum resolution of 18 line pairs per millimeter. Due to the relative low resolution of the target, we used two normal lens with 75mm focal length as the objective lens to achieve a larger FOV. The images obtained by conventional polarizing microscopy and our system are shown below in Fig. 2. All images have the same scale of 400 × 500 μm. As shown in Fig. 2(b), the phase retardation retrieved by our system is a bit more than 1 rad, the standard retardation of 280 nm equals to 1.135 rad when converted to phase retardation around 1550 nm illumination wavelength, which basically matches with our results. As shown in Fig. 2(b)-(h), they are slightly distorted, we thought it would be result from two main causes. Firstly, the resolution between the spectral dispersion direction and the orthogonal scan direction are different. The spectral dispersion direction which corresponding to the vertical direction in the images reconstructed here has a relatively lower resolution than that of the scan direction, so the straight lines paralleled to the scan direction in Fig. 2(b)-(h) distorted more. Secondly, the 10% energy instability of the laser pulses will also result in signal distortion as an amplitude noise. We did not provide the bright field image of the target because of the actual birefringence resolution target is transparent, as shown in Fig. 2(i). Similarly, the M_{11} image in Fig. 2(d) also shows a negligible intensity changing map. The Mueller matrix element M_{11} just represents the complete amplitude transformation property of the sample.

Biomedical Optics EXPRESS

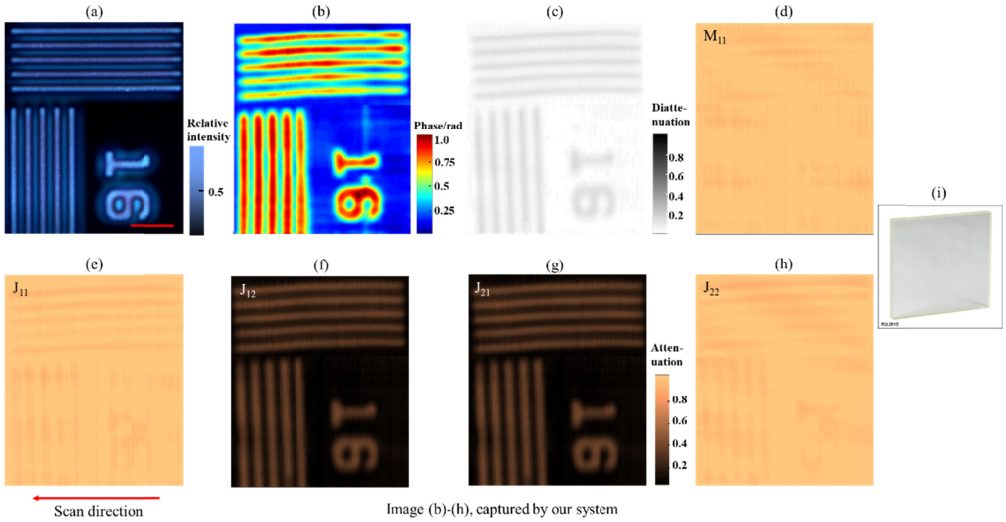

Fig. 2. Images of a standard birefringence target. (a) Image of birefringence captured by the conventional polarizing microscopy. (b) Image of Phase retardation. (c) Image of Diattenuation. (d) Image of Mueller matrix element (M_{11}). (e), (f), (g), (h) Relative amplitude images of the Jones matrix elements ($J_{11} - J_{22}$). (i) Actual image of the birefringence resolution target. Images (d)-(f) share a same color bar All images above have the same dimensions of 400 × 500 μm. Scale bar: 100 μm.

Furthermore, we chose three slice of biological samples to demonstrate the polarization imaging capabilities of our ultrafast polarization imaging system. The first sample is plant stem cross cut, which contains rich birefringence information. The plant stem is a well-organized and important part for nutrients and moisture transportation due to the presence of plant cell wall. The plant cell wall mainly composes of parallelly arranged cellulose structures that enable the cell wall with high stability and crystal properties [34]. Thus, the birefringence of the plant stem can be visually seen under the polarized light microscope, as shown in Fig. 3(a). The bright field (BF) image captured by a conventional optical microscopy is also shown in Fig. 3(b) for comparison. By scanning the biological sample along the direction orthogonal to the 1-D dispersed "spectral rainbow" with a step size of 2 μm, 2-D images of the elements of the Jones matrix can be acquired. The horizontal FOV of the image (approximately 50 μm here) mainly depends on the filtered bandwidth, the groove density of the diffraction grating and the NA of the objective lens, as analyzed in [26]. 250 sample scan were adopted during the experiments, which give rise to a vertical FOV of 500 μm. Figure 3(c) shows the Jones matrix images of the sample, and these images captured at an ultrafast line scan rate up to 100 MHz by our system still shows a good image quality. If a single polarized light based time-stretch imaging system was used, we may only observe an image like J_{11} or J_{22}, which only exhibits partial information along a certain direction (indicated using the green and red arrows, respectively). This observation can be intuitively understood as J_{11} and J_{22} only relates to input and output pulses with the same polarization. However, with the obtained round-trip Jones matrix and equivalent transformed Mueller matrix of the sample taken into consideration, we can retrieve the full amplitude transformation property, and further compute other polarization parameters, such as diattenuation. The image of the Mueller matrix element M_{11} in Fig. 3(d) does show a more complete amplitude transformation property compared to the images of J_{11} or J_{22}. Besides, we calculate the polarization parameters such as the phase retardation and diattenuation through the Eq. (15), and the corresponding images are shown in Fig. 3(e) and (f), respectively. Since the phase retardation is proportional to the birefringence value [35], the phase retardation image (Fig. 3(e)) and the birefringence image (Fig. 3(a)) agree with each other.

Biomedical Optics EXPRESS

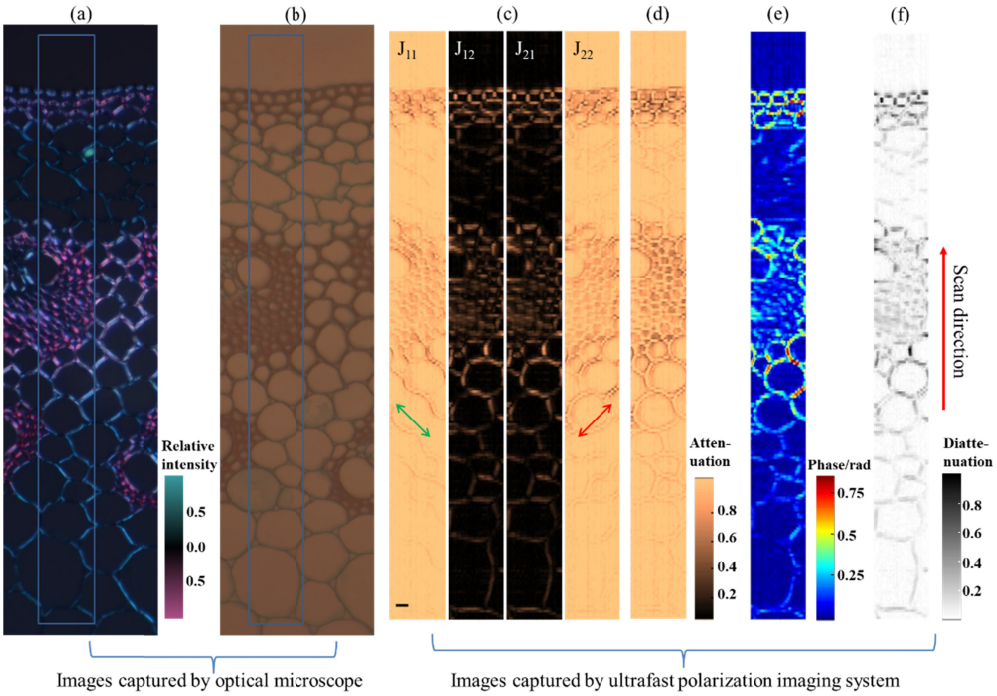

Fig. 3. Images of a plant stem cross cut slice. (a) Image of birefringence captured by the orthogonal polarizing microscopy. (b) Bright field (BF) image captured by the conventional optical microscopy. (c) Relative amplitude of the Jones matrix elements ($J_{11} - J_{22}$). (d) Image of Mueller matrix element (M_{11}). (e) Image of Phase retardation. (f) Image of Diattenuation. All images captured by our system above have the same dimensions of 50 × 500 μm. Scale bar: 10 μm.

The second biological sample is a slice of spirogyra conjugation. Spirogyra is a typical representative of chlorophyta joint algae Spirogyra plants and it is widely distributed in ponds, ditches, rivers, lakes, and paddy fields [36]. It is a nice sample for the observation and studying of algae cell structure and its conjugation. The images acquired by conventional optical microscopy, conventional polarization microscopy, and our ultrafast polarization imaging system are shown in Fig. 4. Again, the M_{11} image in Fig. 4(d) still shows more complete amplitude information especially within the zygospore than the J_{11} or J_{22} image in Fig. 4(c). Besides, the phase retardation image in Fig. 4(e) shows an even more complete and high contrast birefringence information than the birefringence image captured by orthogonal polarizing microscope in Fig. 4(b).

Biomedical Optics EXPRESS

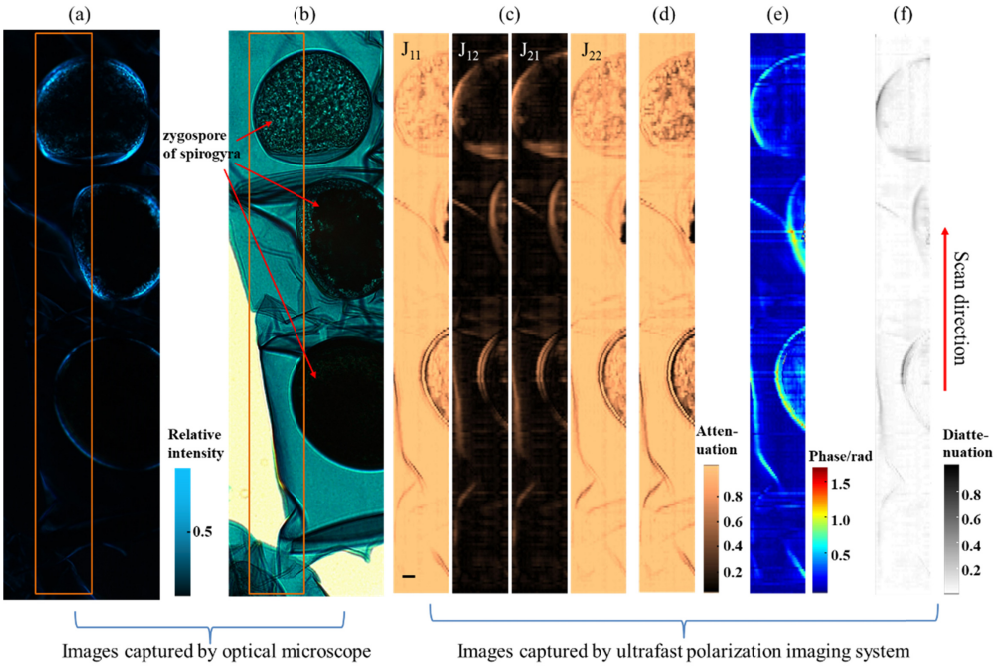

Fig. 4. Images of a spirogyra conjugation slice. (a) Image of birefringence captured by orthogonal polarizing microscopy. (b) Bright field (BF) Image captured by conventional optical microscopy. (c) Images of the relative amplitude of Jones matrix elements (J_{11}-J_{22}). (d) Image of Mueller matrix element (M_{11}). (e) Image of phase retardation. (f) Image of diattenuation. All images captured by our system above have the same dimensions of 50 × 500 μm. Scale bar: 10 μm.

The last sample is a human skin basal cell carcinoma on a glass slide. Basal cell carcinoma (BCC) is the most prevalent skin cancer among Caucasians, and the incidence of BCC continues to increase worldwide. Thus, diagnostic methods with faster speed are need for higher throughput specimen diagnosis. The images of this slice of human skin basal cell carcinoma acquired by conventional optical microscopy and our ultrafast polarization imaging system are shown in Fig. 5. In both the conventional optical microscopy images and our system retrieved images, we can clearly see the phase retardation, diattenuation, and birefringence difference between the above transparent part and below non-transparent part around the connective tissue of this human skin basal cell carcinoma, while this alternation of the connective tissue may still need traditional pathologic analysis to confirm. And still, we can acquire the image of Mueller matrix element M_{11} with a more complete amplitude transformation information than the J_{11} or J_{22} image, which is equivalent to the images obtained using a single polarized time-stretch imaging system. On the other hand, when comparing to the traditional polarizing microscopy, quantitative phase retardation information and decomposition or transformation of the Mueller matrix can be further used in quantitative assessment on the characteristic features of the pathological tissues [37].

Biomedical Optics EXPRESS

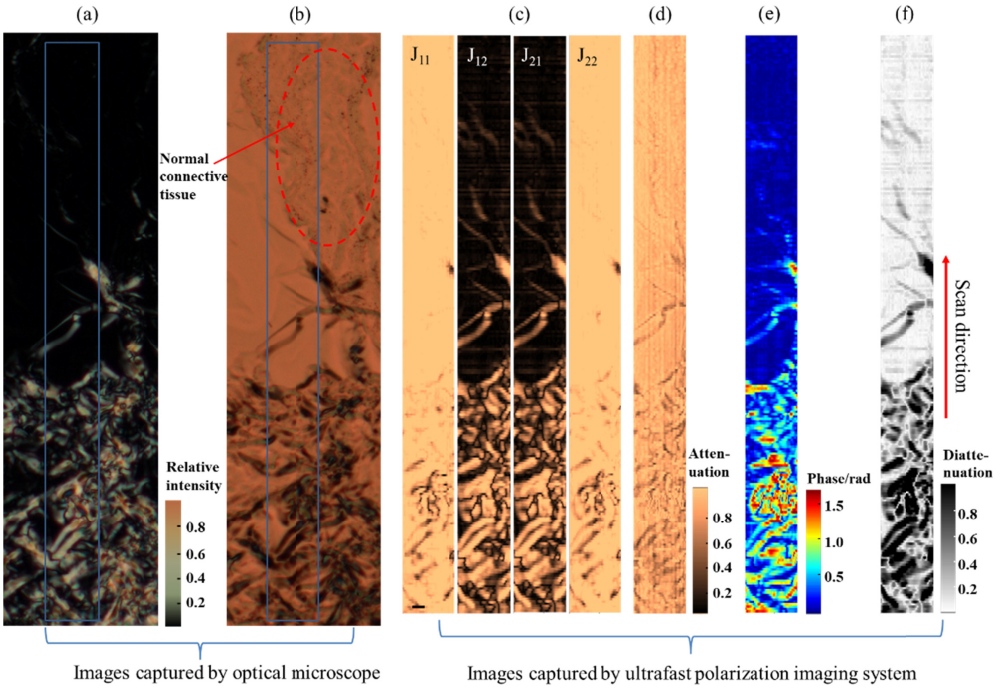

Fig. 5. Images of a human skin basal cell carcinoma slice. (a) Image of birefringence captured by orthogonal polarizing microscopy. (b) Bright field (BF) Image captured by conventional optical microscopy. (c) Images of the relative amplitude of Jones matrix elements (J_{11}-J_{22}). (d) Image of Mueller matrix element (M_{11}). (e) Image of phase retardation. (f) Image of diattenuation. All images captured by our system above have the same dimensions of 50 × 500 μm. Scale bar: 10 μm.

4. Discussion and conclusion

The proposed system is a 1D line scan imaging system, so 2D image acquirement needs vertical shifting. Thus, the actual 2D imaging speed depends on the vertical shifting speed and the imaging vertical length. Here we use electrical moving stage to realize sample vertical shifting, which is a relatively slow method just for experimental demonstration. By using microfluidics or other smart way like mounting serval samples on a designed high speed spinning digital versatile disc (DVD) [20–22], researchers achieved relatively fast 2D imaging and could detect living cells meanwhile. Comparing to conventional visible light based standard polarization microscopy, our system has a relatively lower spatial resolution (~3μm) due to the longer operating wavelength but a much higher temporal resolution (10ns). Additionally, comparing to previous systems, the proposed system can achieve amplitude, phase and polarization such multi-contrast imaging simultaneously. Note that the multi-contrast imaging actually depends on samples. If samples are non-polarization sensitive, the orthogonal polarized lights will carry the same amplitude and phase information, thus no polarization information will be obtained but only phase-sensitive information can be used for reconstruction of depth and refractive index information of the sample [26].

Despite the advantages mentioned above, there are still two main limitations of this ultrafast polarization imaging system. The first main limitation is that it's not applicable for thick samples with high scattering. The reason is that the coherent mechanism utilized here can still detect partial scattered light of the sample if only it reaches the detector. Thus, light scattered by the sample will add an amplitude noise to the measured interference signal. Therefore, the samples we used here are all biology slices with tens of micrometers thickness to avoid light scattering as much as possible. Another limitation of the proposed system is the

Biomedical Optics EXPRESS

imaging recording time length is finite, which is caused by the utilized oscilloscope. In the proposed system here, the line scan imaging data was firstly stored in the memory of the oscilloscope until it's full, and then transmitted to the computer through an Ethernet cable. Due to the limited memory depth of the oscilloscope, the imaging recording time length is finite. This is a drawback of current "off-line" imaging system that was used for experimental demonstration. Actually, an in-line real time imaging system with infinite imaging time length can be realized with embedded hardware processing techniques.

Additionally, as we know, birefringence and diattenuation represent different polarization properties of samples, birefringence shows the refractive index property, and diattenuation shows the transmittance or absorption property when light polarized parallel and polarized perpendicular to an orientation axis. Although diattenuation is negligible in most biological tissues, we can still make it an extension for polarizing imaging [38,39]. In the reference article, diattenuation was used to analysis large or long fibrous protein based biological tissue, such as brain tissue or retinal nerve fiber.

In summary, by combining the optical coherent detection of orthogonal polarizations and time-stretch techniques, we developed a polarization imaging system to image polarization-sensitive information of biological samples with an ultrafast line scanning rate up to 100 MHz. We demonstrated the capability of this imaging system by imaging a standard birefringence resolution target and three slices of different biological samples, including the plant stem cross cut, the spirogyra conjugation, and the skin basal cell carcinoma sample. We anticipate that this ultrafast polarization imaging system will become a feasible approach for imaging ultrafast polarization-sensitive dynamics in future *in vivo* biological and biomedical applications.

Funding

National Natural Science Foundation of China (NSFC) (61705088, 61525502, 61435006, 61775085, 61601199, 61575082, 61490715); Local Innovation and Research Teams Project of Guangdong Pearl River Talents Program (2017BT01X121); The Youth Science and Technology Innovation Talents of Guangdong (2015TQ01X606); Pearl River S&T Nova Program of Guangzhou (201710010051); The Science and Technology Planning Project of Guangdong Province (2017B010123005).

Disclosures

The authors declare that there are no conflicts of interest related to this article.

References

1. S. G. Demos and R. R. Alfano, "Optical polarization imaging," Appl. Opt. **36**(1), 150–155 (1997).
2. L. Wang and H. I. Wu, *Biomedical Optics: Principles and Imaging* (John Wiley & Sons, 2012), Chap. 1.
3. S. L. Jacques, J. C. Ramella-Roman, and K. Lee, "Imaging skin pathology with polarized light," J. Biomed. Opt. **7**(3), 329–340 (2002).
4. N. Ghosh and I. A. Vitkin, "Tissue polarimetry: concepts, challenges, applications, and outlook," J. Biomed. Opt. **16**(11), 110801 (2011).
5. R. S. Gurjar, V. Backman, L. T. Perelman, I. Georgakoudi, K. Badizadegan, I. Itzkan, R. R. Dasari, and M. S. Feld, "Imaging human epithelial properties with polarized light-scattering spectroscopy," Nat. Med. **7**(11), 1245–1248 (2001).
6. W. Groner, J. W. Winkelman, A. G. Harris, C. Ince, G. J. Bouma, K. Messmer, and R. G. Nadeau, "Orthogonal polarization spectral imaging: a new method for study of the microcirculation," Nat. Med. **5**(10), 1209–1212 (1999).
7. V. V. Tuchin, L. V. Wang, and D. A. Zimnyakov, *Optical Polarization in Biomedical Applications* (Springer Science & Business Media, 2006).
8. J. C. Low, T. J. Ober, G. H. McKinley, and K. M. Stankovic, "Quantitative polarized light microscopy of human cochlear sections," Biomed. Opt. Express **6**(2), 599–606 (2015).
9. A. M. Vrabioiu and T. J. Mitchison, "Structural insights into yeast septin organization from polarized fluorescence microscopy," Nature **443**(7110), 466–469 (2006).
10. Y. Kim, J. Jeong, J. Jang, M. W. Kim, and Y. Park, "Polarization holographic microscopy for extracting spatio-temporally resolved Jones matrix," Opt. Express **20**(9), 9948–9955 (2012).

Biomedical Optics EXPRESS

11. M. Sun, H. He, N. Zeng, E. Du, Y. Guo, S. Liu, J. Wu, Y. He, and H. Ma, "Characterizing the microstructures of biological tissues using Mueller matrix and transformed polarization parameters," Biomed. Opt. Express **5**(12), 4223–4234 (2014).
12. J. J. Pasquesi, S. C. Schlachter, M. D. Boppart, E. Chaney, S. J. Kaufman, and S. A. Boppart, "In vivo detection of exercised-induced ultrastructural changes in genetically-altered murine skeletal muscle using polarization-sensitive optical coherence tomography," Opt. Express **14**(4), 1547–1556 (2006).
13. P. J. Campagnola and L. M. Loew, "Second-harmonic imaging microscopy for visualizing biomolecular arrays in cells, tissues and organisms," Nat. Biotechnol. **21**(11), 1356–1360 (2003).
14. J. N. Forkey, M. E. Quinlan, and Y. E. Goldman, "Protein structural dynamics by single-molecule fluorescence polarization," Prog. Biophys. Mol. Biol. **74**(1-2), 1–35 (2000).
15. C. T. Anderson, A. Carroll, L. Akhmetova, and C. Somerville, "Real-time imaging of cellulose reorientation during cell wall expansion in Arabidopsis roots," Plant Physiol. **152**(2), 787–796 (2010).
16. T. Tani, M. Shribak, and R. Oldenbourg, "Living cells and dynamic molecules observed with the polarized light microscope: the legacy of Shinya Inoue," Biol. Bull. **231**(1), 85–95 (2016).
17. D. Litwiller, "Ccd vs. cmos," Photon. Spectra **35**(1), 154–158 (2001).
18. K. Goda, K. K. Tsia, and B. Jalali, "Serial time-encoded amplified imaging for real-time observation of fast dynamic phenomena," Nature **458**(7242), 1145–1149 (2009).
19. A. K. Lau, T. T. Wong, K. K. Ho, M. T. Tang, A. C. Chan, X. Wei, E. Y. Lam, H. C. Shum, K. K. Wong, and K. K. Tsia, "Interferometric time-stretch microscopy for ultrafast quantitative cellular and tissue imaging at 1 μm," J. Biomed. Opt. **19**(7), 76001 (2014).
20. A. K. Lau, H. C. Shum, K. K. Wong, and K. K. Tsia, "Optofluidic time-stretch imaging - an emerging tool for high-throughput imaging flow cytometry," Lab Chip **16**(10), 1743–1756 (2016).
21. H. Kobayashi, C. Lei, Y. Wu, A. Mao, Y. Jiang, B. Guo, Y. Ozeki, and K. Goda, "Label-free detection of cellular drug responses by high-throughput bright-field imaging and machine learning," Sci. Rep. **7**(1), 12454 (2017).
22. A. H. Tang, P. Yeung, G. C. Chan, B. P. Chan, K. K. Wong, and K. K. Tsia, "Time-stretch microscopy on a DVD for high-throughput imaging cell-based assay," Biomed. Opt. Express **8**(2), 640–652 (2017).
23. T. Y. Li, A. E. Willner, and I. Kaminow, *Optical Fiber Telecommunications VB: Systems and Networks* (Elsevier, 2010), Chap. 3.
24. T. D. Yang, K. Park, Y. G. Kang, K. J. Lee, B. M. Kim, and Y. Choi, "Single-shot digital holographic microscopy for quantifying a spatially-resolved Jones matrix of biological specimens," Opt. Express **24**(25), 29302–29311 (2016).
25. D. G. Anderson and R. Barakat, "Necessary and sufficient conditions for a Mueller matrix to be derivable from a Jones matrix," J. Opt. Soc. Am. A **11**(8), 2305–2319 (1994).
26. Y.-H. Feng, X. Lu, L. Song, X. Guo, Y. Wang, L. Zhu, Q. Sui, J. Li, K. Shi, and Z. Li, "Optical digital coherent detection technology enabled flexible and ultra-fast quantitative phase imaging," Opt. Express **24**(15), 17159–17167 (2016).
27. K. K. Tsia, K. Goda, D. Capewell, and B. Jalali, "Performance of serial time-encoded amplified microscope," Opt. Express **18**(10), 10016–10028 (2010).
28. N. Vansteenkiste, P. Vignolo, and A. Aspect, "Optical reversibility theorems for polarization: application to remote control of polarization," J. Opt. Soc. Am. A **10**(10), 2240–2245 (1993).
29. B. H. Park, M. C. Pierce, B. Cense, and J. F. de Boer, "Jones matrix analysis for a polarization-sensitive optical coherence tomography system using fiber-optic components," Opt. Lett. **29**(21), 2512–2514 (2004).
30. E. Ip, A. P. T. Lau, D. J. Barros, and J. M. Kahn, "Coherent detection in optical fiber systems," Opt. Express **16**(2), 753–791 (2008).
31. M. Yamanari, S. Makita, V. D. Madjarova, T. Yatagai, and Y. Yasuno, "Fiber-based polarization-sensitive Fourier domain optical coherence tomography using B-scan-oriented polarization modulation method," Opt. Express **14**(14), 6502–6515 (2006).
32. S. Jiao and L. V. Wang, "Jones-matrix imaging of biological tissues with quadruple-channel optical coherence tomography," J. Biomed. Opt. **7**(3), 350–358 (2002).
33. S.-Y. Lu and R. A. Chipman, "Homogeneous and inhomogeneous Jones matrices," J. Opt. Soc. Am. A **11**(2), 766–773 (1994).
34. U. P. Agarwal, "Raman imaging to investigate ultrastructure and composition of plant cell walls: distribution of lignin and cellulose in black spruce wood (Picea mariana)," Planta **224**(5), 1141–1153 (2006).
35. N. Kemp, H. Zaatari, J. Park, H. G. Rylander Iii, and T. Milner, "Form-biattenuance in fibrous tissues measured with polarization-sensitive optical coherence tomography (PS-OCT)," Opt. Express **13**(12), 4611–4628 (2005).
36. G. F. Leedale, B. J. D. Meeuse, and E. G. Pringsheim, "Structure and physiology of Euglena spirogyra. I and II," Arch. Microbiol. **50**(1), 68–102 (1965).
37. C. He, H. He, J. Chang, Y. Dong, S. Liu, N. Zeng, Y. He, and H. Ma, "Characterizing microstructures of cancerous tissues using multispectral transformed Mueller matrix polarization parameters," Biomed. Opt. Express **6**(8), 2934–2945 (2015).
38. X. R. Huang and R. W. Knighton, "Diattenuation and polarization preservation of retinal nerve fiber layer reflectance," Appl. Opt. **42**(28), 5737–5743 (2003).
39. M. Menzel, J. Reckfort, D. Weigand, H. Köse, K. Amunts, and M. Axer, "Diattenuation of brain tissue and its impact on 3D polarized light imaging," Biomed. Opt. Express **8**(7), 3163–3197 (2017).